Hyperspectral remote sensing and geological applications

D. Ramakrishnan* and Rishikesh Bharti

Department of Earth Sciences, Indian Institute of Technology Bombay, Powai, Mumbai 400 076, India

This article reviews the potential of Hyperspectral Remote Sensing (HRS) technique in various geological applications ranging from lithological mapping to exploration of economic minerals of lesser crustal abundance. This work updates understanding on the subject starting from spectroscopy of minerals to its application in exploring mineral deposits and hydrocarbon reservoirs through different procedures such as atmospheric correction, noise reduction, retrieval of pure spectral endmembers and unmixing. Besides linear unmixing, nonlinear unmixing and parameters attributed to nonlinear behaviour of reflected light are also addressed. A few case studies are included to demonstrate the efficacy of this technique in different geological explorations. Finally, recent developments in this field like ultra spectral imaging from unmanned aerial vehicles and its consequences are pointed out.

Keywords: Geological applications, hyperspectral remote sensing, spectroscopy of minerals and rocks, spectral unmixing.

Introduction

MINERAL exploration and geological mapping through conventional geological techniques are tedious, expensive and time-consuming. Mapping and targeting an economic deposit through traditional techniques involves extensive fieldwork, structural mapping, study of landforms, petrography, mineralogy and geochemical analyses[1,2]. These techniques need a strong laboratory database to discern slight variation in composition of ore grades. With the advent of multispectral sensors (e.g. ASTER, Landsat) having bands in the Shortwave Infrared (SWIR) and Thermal Infra-Red (TIR) regions, lithological discrimination and mineral potential mapping were possible from space/airborne platforms[3–5]. However, detailed understanding on precise mineral composition and relative abundance of constituents within Field of View (FOV) was not possible with these data due to coarse bandwidth and poor spectral contiguity. However, when spectroscopy, radiometry and imaging techniques were bundled as imaging spectroscopy, limitations of multispectral remote sensing were overcome. The hyperspectral sensors on the other hand, are capable of acquiring images in 100–200 contiguous spectral bands. This ability to acquire laboratory-like spectra from an air/spaceborne sensor is a major breakthrough in remote sensing[6]. As a result, hyperspectral sensors provide a unique combination of both spatially and spectrally contiguous images that allow precise identification of minerals[6]. Over the last two decades, mineral mapping and lithological discrimination using airborne hyperspectral sensors like AVIRIS, HYDICE, DAIS, HyMAP have been extensively attempted[7,8]. However, launch of NASA's EO-1 Hyperion sensor with 242 spectral bands in 0.4–2.5 μm range marked a new beginning in spaceborne mineral potential mapping.

In this article a comprehensive review of spectroscopy of minerals and rocks, importance of field spectroscopy, and challenges in analyses of hyperspectral data for geological exploration are discussed.

*For correspondence. (e-mail: ramakrish@iitb.ac.in)

Reflectance and emission spectroscopy of minerals and rocks

Since Newton's discovery of composite nature of white light in 1664, spectroscopy in all ranges of wavelength has been used to study properties of terrestrial and extraterrestrial objects[9]. When light interacts with a mineral or rock, certain wavelength regions of incident light are absorbed, some are reflected, and some are transmitted depending on the chemistry and crystal structure. Absorption of energy in minerals results from electronic and vibration processes of molecules[6,10,11]. The electronic processes include crystal field effects, charge transfers, conduction bands and colour centres[12,13].

The vibrational processes involving stretching, bending and rotation offer information about functional groups. Molecular vibration-related spectral absorption is characteristic of functional groups and is useful in identifying minerals. Absorption features related to fundamental, overtone and combination manifest in the 1–30 μm region. Spectral absorption features of minerals (such as silicates, oxides, hydroxides, carbonates, sulphides, nitrates and borates) are well established (Figures 1–3) and identification of these minerals based on spectra is now possible[14–20]. These studies on reflectance and emission spectroscopy of minerals lead to generation and archival of exhaustive spectral library.

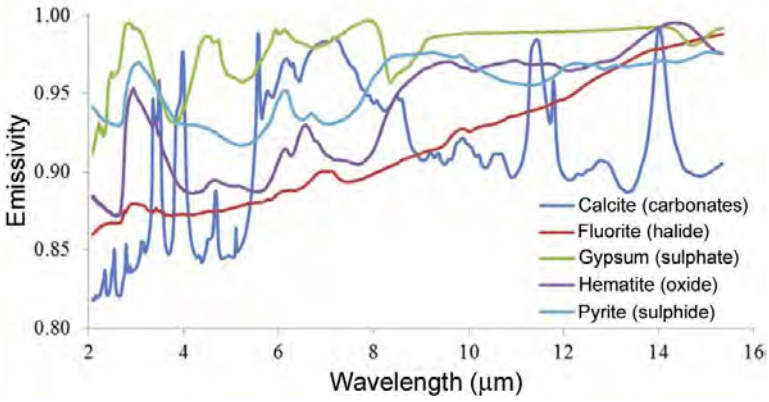

Figure 1. SWIR–TIR spectral plots for minerals representing different functional groups.

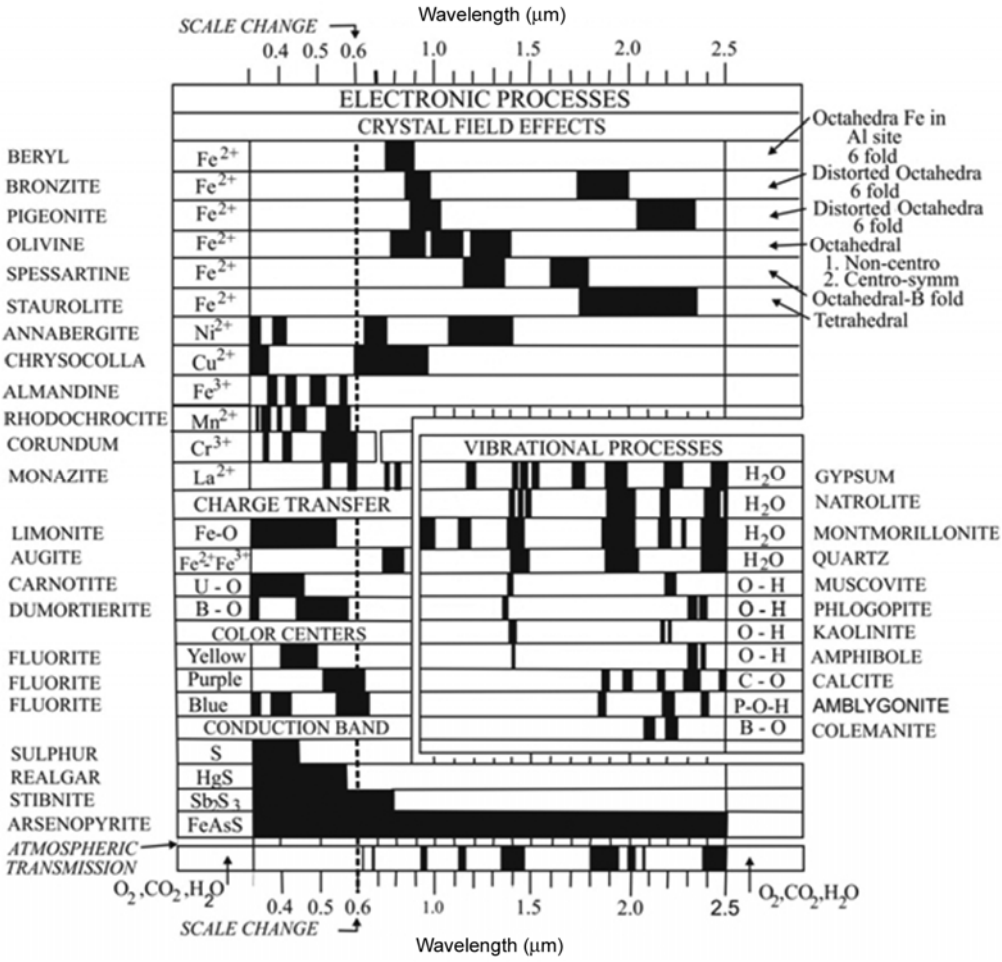

Figure 2. Spectral absorption positions for various minerals (after Hunt[17]).

Subsequently, it was realized that spectral database generated using pure minerals and rocks in the laboratory has limited application potential for exploration due to inherent heterogeneity and associated spectral mixing. This led to the development of field spectroscopy, wherein field-related natural heterogeneities are addressed. With the advent of compact and sophisticated spectrometers and spectroradiometers, field spectroscopy is evolving as a robust technique in mineral exploration and geological mapping[21–23] and is extensively used from initial reconnaissance to ore-grade evaluation through intermediate stages such as drilling, assay estimation and

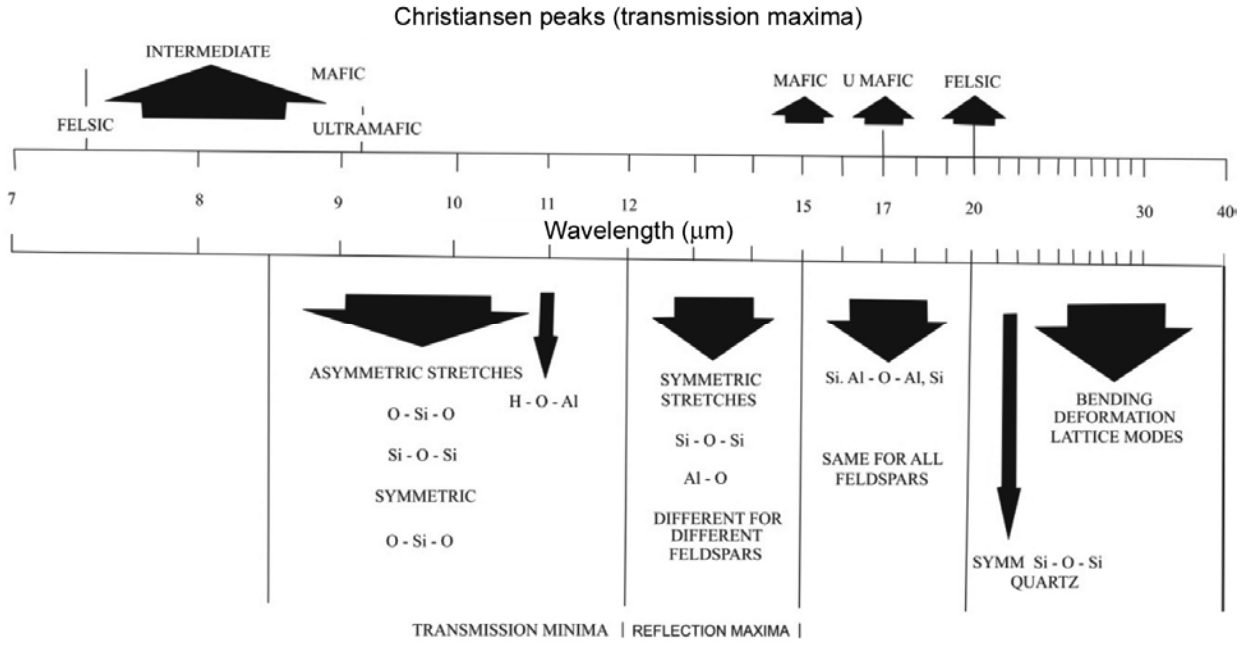

Figure 3. Regions of spectral absorption for silicate minerals and rocks (after Hunt[18]).

Table 1. List of alteration minerals and metallogenic environments (after Thompson and Thompson[26]).

Metallogenic environment	Alteration zone name	Characteristic SWIR active mineral assemblages
Massive sulphide	Tourmaline	Muscovite and tourmaline
	Carbonate	Siderite, ankerite, calcite
	Sericite	Chlorite and sericite
	Albite	Chlorite, biotite, muscovite
Mesothermal	Carbonate	Calcite, ankerite, dolomite, muscovite
	Chlorite	Chlorite, muscovite and actinolite
	Biotite	Chlorite and biotite
Low- and high-sulphide epithermal	Propylitic	Epidote, chlorite, sericite, calcite, illite, smectite, montmorillonite
	Argillic	Kaolinite, dickite, alunite, diaspore, pyrophyllite, jarosite
	Adularia	Sericite, illite–smectite, kaolinite, chalcedony, opal, montmorillonite, calcite, dolomite
Igneous intrusion related	Potassic	Phlogopite, actinolite, sericite, chlorite, epidote, muscovite, anhydrite
	Sodic	Actinolite, diopside, chlorite, epidote, scapolite
	Phyllic	Muscovite–illite, chlorite, anhydrite
	Argillic	Pyrophyllite, sericite, diaspore, alunite, topaz, tourmaline, kaolinite, montmorillonite, calcite
	Greisen	Topaz, muscovite, tourmaline
	Skarn	Clinopyroxene, wollastonite, actinolite–tremolite, vesuvianite, epidote, serpentinite–talc, calcite, chlorite, illite–smectite, nontronite
Supergene sulphide	Oxidized and leached zones	Clay minerals, limonite, goethite, hematite, jarosite
	Enriched zone	Chalcocite, covellite, chrysocolla, native copper and copper oxide, carbonate and sulphate minerals

core logging. Field spectroscopy in the TIR region is relatively new and has tremendous application in lithological mapping and mineral exploration[24,25].

From exploration perspective, mineral deposits that can be easily targeted using reflectance spectra include epithermal gold, low-, and high-sulphidation deposits; porphyries, kimberlites, iron oxide, copper, gold, skarns and uranium. Table 1 summarizes a list of pathway minerals that are active in the SWIR region, which can be easily identified by HRS technique[26].

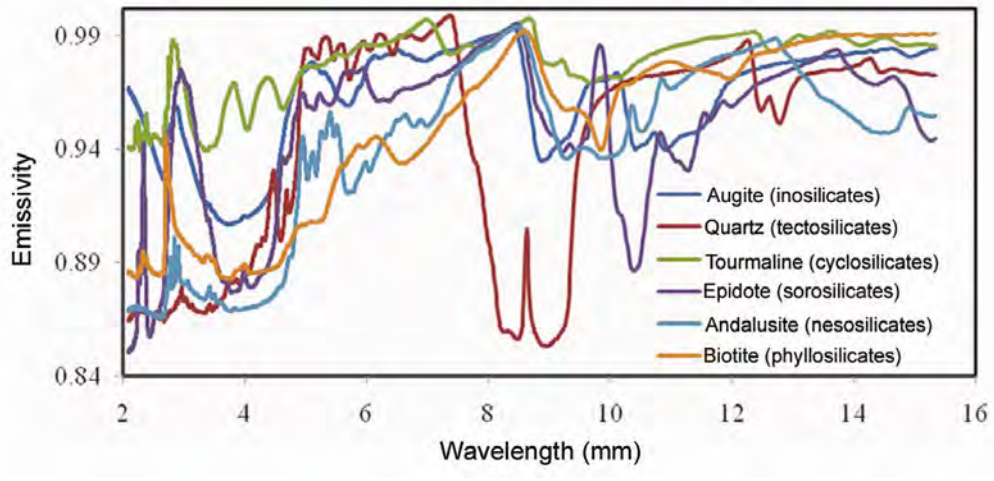

Figure 4. Spectra (2–16 μm) representing most important class of rock-forming minerals.

Field spectroscopy

Application of field spectroscopy in geo-exploration predates airborne spectrometry, as it is essential to acquire accurate ground data on spectral reflectance/emission. Compared to the first ever Portable Field Reflectance Spectrometer (PFRS), present-day field spectroradiometers are far advanced in terms of spectral range, resolution and signal-to-noise ratio. Now, both reflectance and emission spectral measurements of *in situ* rocks can be made from 0.35 to 14.00 μm (Figure 4). Evolution of field spectroscopy over the past four decades can be well visualized from the works of Slater[27], Milton[28], and Milton *et al.*[29].

From geological perspective, field spectroscopy can be employed in two different modes. First, it can be used as a stand-alone method to decipher mineralogy and lithology at field/mine scale. Ramakrishnan *et al.*[2] employed this method to delineate Pb–Cu–Zn mineralization and associated alteration zones. They used field spectra, spectral library and unmixing algorithms to identify ore zones and rock types in the field. Kurz[30] adopted close-range hyperspectral imaging and lidar to map diagenetic carbonate and clastic carbonates in the field. Secondly, it can be used in ore grade assessment; mine face mapping and ore blending. Hyperspectral logging, popularly called as 'HyLogging' involves estimation of continuous assay/grade details based on spectral information collected from cores, run-off mine ores and mine faces[31,32].

When field spectroscopy is used in conjunction with air/spaceborne hyperspectral image cubes, scaling-up of spectral details becomes necessary. This includes measuring spectral properties of individual scene elements, modelling cumulative effects of scene elements, and vicarious calibration of air/spaceborne data to match spatial scale of field data[33,34]. Critical issues affecting scaling of field spectral information to air/spaceborne measurements[35] include reliability of spectral measurements, spatial sampling strategy, sensitivity of equipment and dynamic field conditions. Apart from the above parameters, texture, fabric and source–sensor geometry also have a strong influence on intensity of reflectance/emission spectra[36,37].

Spectral library and pre-processing of spectra

Generation of a well-characterized spectral repository and understanding spectral features of minerals and rocks is the most important aspect of HRS. The United States Geological Survey (USGS) spectral library[38] contains reflectance spectra of minerals and rocks from ultraviolet (0.35 μm) to SWIR regions (2.5 μm). The John Hopkins University (JHU) spectral library[20] includes reflectance spectra of minerals from 2 to 25 μm regions. The JHU spectral library has been generated using integrating spheres for measurement of directional hemispherical reflectance. The Jet Propulsion Laboratory (JPL) spectral library published reflectance spectra of 160 minerals, from 0.4 to 2.5 μm. Data for 135 of the minerals are presented at three different grain sizes, namely 125–500, 45–125 and <45 μm. ASTER spectral library is a compendium of data from JPL, JHU and USGS libraries in a standard data format. A library of thermal infrared emission spectra of minerals was prepared by Arizona State University (ASU) for planetary exploration purpose[39]. A new spectral library, Emission and Reflectance Spectral Library (EARSL) of rock-forming minerals and common rocks has been compiled by the Council of Industrial Research Organisation (CSIRO), Australia. Reflectance Experiment Laboratory (RELab) spectral library of minerals and rocks includes bidirectional reflectance spectra of the Earth and other planetary materials. Since the above spectral database differs in terms of source–sensor geometry, sampling rate and spectral spread, normalization is necessary for any practical applications[40].

Imagining spectroscopy from air and space

Image pre-processing and spectral unmixing

HRS requires an elaborate sequence of data processing. The first step involves removal of atmospheric effects and transformation of remotely measured radiance to ground reflectance/emissivity values. Since 1980s, atmospheric correction algorithms have evolved from statistical/empirical-based approaches to recent radiative transfer (RT)-based approaches. Salient among the algorithms include Flat Field (FF)[41], Internal Average Relative Reflectance (IARR)[42], Empirical Line Calibration (ELC)[43] and RT-based approaches[44] such as Atmosphere REMoval (ATREM)[45], High-accuracy Atmospheric Correction for Hyperspectral Data (HATCH)[46], Atmosphere CORrection Now (ACORN)[47], Fast Line-of-sight Atmospheric Analysis of Spectral Hypercubes (FLAASH)[48], Imaging Spectrometer Data Analysis System (ISDAS)[49], and Atmospheric and Topographic Correction (ATCOR)[50].

Once corrected for atmospheric effects, the data need to be processed for dimensionality. Minimum Noise Fraction (MNF)[51] algorithm is being widely used for noise reduction and dimensionality reduction. Besides MNF, techniques like Independent Component Analysis (ICA)[52], Orthogonal Sub-Space Projection (OSP)[53], and Convex Cone Analysis (CCA)[54] are important. Due to coarse spatial resolution, heterogeneity of natural surfaces and multiple scattering effects, reflectance/emission spectrum measured by a hyperspectral sensor is always a spectral mixture[55]. A mixed pixel is a pixel which combines radiance values of multiple ground materials. On the contrary, a pure pixel represents radiance values of a single material. Such pure spectral signatures in an image are referred to as endmembers[55]. However, image endmembers are often a mixture of several library minerals. Hyperspectral unmixing involves two cascading steps. In the first stage, the image is classified based on image-derived endmembers and in the second stage, endmembers are resolved for mineralogy using spectral library. Since this procedure resolves each pixel in terms of mineral combinations mixed in various proportions, spectral unmixing is called as sub-pixel classification. The most popular model for spectral unmixing is linear mixing model (LMM)[55,56].

The basic assumption of LMM (eq. (1)) is that every pixel in an image is a combinations of one or more combinations of endmembers. Many endmember/pure pixel detection algorithms like N-Finder[57] and Pixel Purity Index (PPI)[58] are based on this concept. Other endmember retrieval algorithms include Automated Morphological Endmember Extraction (AMEE)[59], Spatial–Spectral Endmember Extraction (SSEE) algorithm, Vertex Component Analysis (VCA)[56], and Minimum Volume Transform and Convex Cone Analysis (MVTCC)[60]. Unmixing of image spectra as a linear combination of library/field spectra was attempted by several researchers for mineral identification and estimation of their abundance[61–63].

$$R_k = \sum_i^n E_{i,k} x_i + \varepsilon_k, \tag{1}$$

where R is the reflectance of source at wavelength k; E the reflectance of endmember i at wavelength k; x the abundance of endmember i and ε is the error at wavelength k.

Often efficiency of spectral unmixing is estimated by Root Mean Squared Error (RMSE) between test and modelled spectra.

$$\text{RMSE} = \sqrt{\left(\sum_{k=1}^{m} \varepsilon_k^2\right) \Big/ m}, \tag{2}$$

where RMSE is root mean square error of ε_k; n the number of endmembers, and m is the number of wavelength channels in the discrete spectrum.

LMM is based on the assumption of single scattering of light. However, in most natural situations, reflection process involves multiple scattering and hence LMM is not effective. Therefore, nonlinear spectral unmixing model based on Radiative Transfer Equation (RTE) is necessary to understand influencing factors and effects associated with multiple scattering. Using fundamental principles of radiative transfer theory, Hapke and Wells[64] derived an analytical equation for bidirectional reflectance function (BRF) of a medium composed of granular particles and applied it to planetary surfaces (e.g. Moon, Mars). These equations consist of several parameters which account for single and multiple scattering for an intimate mixture of minerals. This model is based on assumptions that (i) particle size is very large compared to wavelength of light measuring it; (ii) isotropic single and multiple scatterers represent the mixture, and (iii) angle of source and sensor are well defined from the vertical[64]. It is considered that radiance received at the detector is composed of singly scattered radiance I_s and multiple scattered radiance I_m for the given total irradiance J. Hence I represents cumulative effect of single and multiple scattered components ($I = I_s + I_m$). Considering angle of light incidence ($I(\theta_i)$), emergence ($e(\theta_r)$), and azimuth angle (r), Hapke[65] calculated photometric function for bidirectional reflectance (R_c) using the relationship

$$R_c(i, e, \psi) = \frac{I}{J} = \frac{w}{4\pi} \frac{\mu_0}{\mu_0 + \mu} \times \{[1 + B(g)]P(g, g') + H(\mu_0)H(\mu) - 1\}S(\theta). \tag{3}$$

Here μ_0 and μ are cosines of incidence $i(\theta_i)$ and emergence $e(\theta_r)$ angles; g the phase angle; w the wavelength

(λ)-dependent single scattering albedo; $B(g)$ the opposition effect function; $P(g)$ the phase function and $H(\mu)$ is the multiple scattering function. Function for macroscopic roughness $S(\theta)$ is also referred to as topographic shadowing function[66]. Parameter θ is a mean topographic slope angle that provides a measure of surface macroscopic roughness of a pixel (shape and roughness of particles). If target spectra are from a terrain with small-scale roughness, then $S(\theta)$ is initialized to unity[66]. Shepard and Campbell[67] suggested that the scale of the smallest facet is the dominant scale for surface shadowing. In case of larger grain sizes, θ parameter increases depending on geological properties[68]. It alters local incidence and emergence angles. Single scattering albedo (w) can be calculated from measured reflectance using eq. (4)

$$w = \frac{4r_0}{(1+r_0)^2}, \tag{4}$$

where r_0 is the diffuse reflectance. The function of isotropic multiple scattering $H(y)$ includes angle of incidence, emergence and single scattering albedo w

$$H(y) = \frac{1+2y}{1+2\sqrt{1-wy}}, \tag{5}$$

where y is μ_0 or μ. While deriving the solution for radiative transfer equation for an intimate mixture of minerals, effect of decreasing inter-particle spacing has to be taken into consideration. To account for such effects, Hapke *et al.*[69] introduced another function in the reflectance equation, which is known as backscatter function ($B(g)$). It takes into account Shadow Hiding Opposition Effect (SHOE)[69] as

$$B(g) = \frac{B_0}{1+\frac{\tan(g/2)}{h}}. \tag{6}$$

Parameter h in the above equation characterizes compaction of regolith and its particle size distribution. The angular width parameter h is constrained between 0 and 1. An empirical parameter B_0 defines amplitude of opposition effect, with values constrained between 0 and 1. If particles are opaque, scattered light is from the surface and hence B_0 will be equal to 1 (ref. 70). Henyey and Greenstein[71] introduced a phase function by variation of parameters, $-1 \le g,\ g' \le 1$, which ranges from backscattering through isotropic scattering to forward scattering. *H–G* function has a simple expansion in terms of Legendre polynomials. In order to generalize description of fine grain directional reflectance, Jacquemoud *et al.*[72] have modified phase function ($P(g, g')$) as

$$P(g,g') = 1 + b\cos(g) + \frac{c(3\cos^2(g)-1)}{2} + b'\cos(g') + \frac{c'(3\cos^2(g')-1)}{2}. \tag{7}$$

The function $P(g, g')$ includes four Legendre parameters linked with material properties and constrained at intervals b[–2, 2], c[–1, 1], b'[–2, 2] and c'[–1, 1]. Here b determines phase function form and c determines nature of scattering ($c < 0$ corresponds to forward scattering and $c > 0$ to backward scattering). $\cos(g)$ and $\cos(g')$ can be evaluated with values of i, e and ψ using equations

$$\cos(g) = \cos(i)\cos(e) + \sin(i)\sin(e)\cos(\psi)$$

$$\cos(g') = \cos(i)\cos(e) - \sin(i)\sin(e)\cos(\psi). \tag{8}$$

Geological applications

Since the last two decades, HRS has been effectively used in several geological applications such as lithological mapping and exploration of non-metals[2,31,73–75], precious and or economic minerals[76–80], hydrocarbon deposits[81] and also in quality control and grade assessments[31]. Development and successful implementation are detailed below.

Lithological mapping and exploration of industrial minerals

Though HRS in the VNIR–SWIR region is being used for lithologic mapping in various climatic[82] and litho-tectonic terrane (granite[83], ophiolites[84], peridotites[85] and kimberlite[86]), there exists serious limitations as most of the rock-forming minerals are inactive in this region. Since spectral features in the SWIR region are mostly related to overtones and combinations of vibrations of Al–OH, Fe–OH, and Mg–OH, the VNIR–SWIR region is at the most useful for mapping alteration minerals, carbonates and regoliths[87]. Mineral spectral features in the TIR region are mostly attributed to fundamental vibrations (bends and stretches) of Si–O bonds. Thus, the TIR region spectrum is useful for characterizing spectral features of many rock-forming minerals such as quartz, feldspar, amphibole, olivine, mica and pyroxene[88]. Efficacy of the TIR region in lithological mapping has been demonstrated by Zhang and Pazner[8], wherein lithology of Chocolate Mountains area, USA was mapped using ASTER TIR bands and Hyperion datasets. Merucci *et al.*[89] also reported similar results while mapping the lithology of Solfatara crater, Italy using DAIS data. Vaughan *et al.*[90] used TIR hyperspectral imager, Spatially Enhanced Broadband Array Spectrograph System (SEBASS), to map lithology

of Steamboat Springs and Geiger Grade areas, Neveda, USA.

In case of evaporate deposits, the VNIR spectrum exhibits absorption features at 1.5, 1.74, 1.94, 2.03, 2.22 and 2.39 μm and can be easily mapped with Hyperion data[78]. Kurz *et al.*[91] used HRS in the VNIR–SWIR region to discriminate different carbonate lithologies (limestone, karst and hydrothermal dolomites). Based on shift in carbonate absorption feature in the 2.3 μm region, they discriminated different types of limestone. Mapping of sulphate minerals (gypsum, jarosite) using spectral absorption in 1.4, 1.9 and 2.4–2.5 μm absorption bands is being extensively used among terrestrial and planetary remote sensing communities[92,93].

Mapping hydrothermal alteration zones and associated metal deposits

Understanding composition and spatial distribution of alteration mineral assemblages is important in exploring different types of hydrothermal ore deposits. Hydrothermal alteration zones contain complex mixtures of primary mineral assemblages and new minerals formed through interaction of primary assemblage and hydrothermal fluids.

Volcanogenic Massive Sulphide (VMS) deposits: VMS ore deposits are formed due to volcanism-related hydrothermal activities in submarine environments. These deposits are the main source for Cu, Zn, Pb, Au and Ag ores. Alteration haloes developed by VMS deposits are conical in shape, zoned and can be mapped easily. Alteration mineral assemblages of VMS from core to fringe include, a silica alteration zone (comprising complete silica replacement of host rocks, and associated with ore minerals such as sphalerite, galena, chalcopyrite, and pyrite); a chlorite zone (consisting chlorite ± sericite ± silica); a sericite zone (consisting of sericite ± chlorite ± silica) and a silicification zone (comprising minerals related to silica–albite metasomatism).

Pilbara craton, Australia is one of the best VMS-type deposits and is extensively studied from the mineralization perspective[94]. Van Ruitenbeek *et al.*[95] studied this deposit using airborne and field hyperspectral techniques for the distribution of white mica minerals (Figure 5). For this purpose, white mica mineral abundance and distribution maps were prepared using HRS technique and compared with published hydrothermal alteration maps. Based on the Al content, three different zones were identified, namely (i) Al-rich white mica zones, (ii) Al-poor white mica zones predominantly related to K alteration by more evolved hydrothermal fluids, and (iii) high to intermediate Al-content white mica zones related to intense alteration by laterally flowing and upwelling evolved fluids. This work demonstrated the potential of HRS in mapping the distribution of white mica minerals, characterization of hydrothermal systems and reconstruction of palaeo-fluid pathways. Similar application of hyperspectral technique in mapping VMS deposits is reported from different parts of the globe[77].

Hydrothermal epigenetic deposits: This includes fractional granitoid associated (e.g. tin, tungsten, molybdenum), porphyry (e.g. copper, gold), iron oxide, copper, gold and carbonate-hosted strata bound (e.g. lead, zinc) and unconformity-related uranium deposits. Dominant alteration minerals associated with Sn–W mineralization are quartz, albite, muscovite, topaz, pyrite and clay minerals. They occur in greisenized and albitized zones that range in thickness from a few millimetres to 10 cm. Hoefen *et al.*[96] has used HyMap data over Daykundi area,

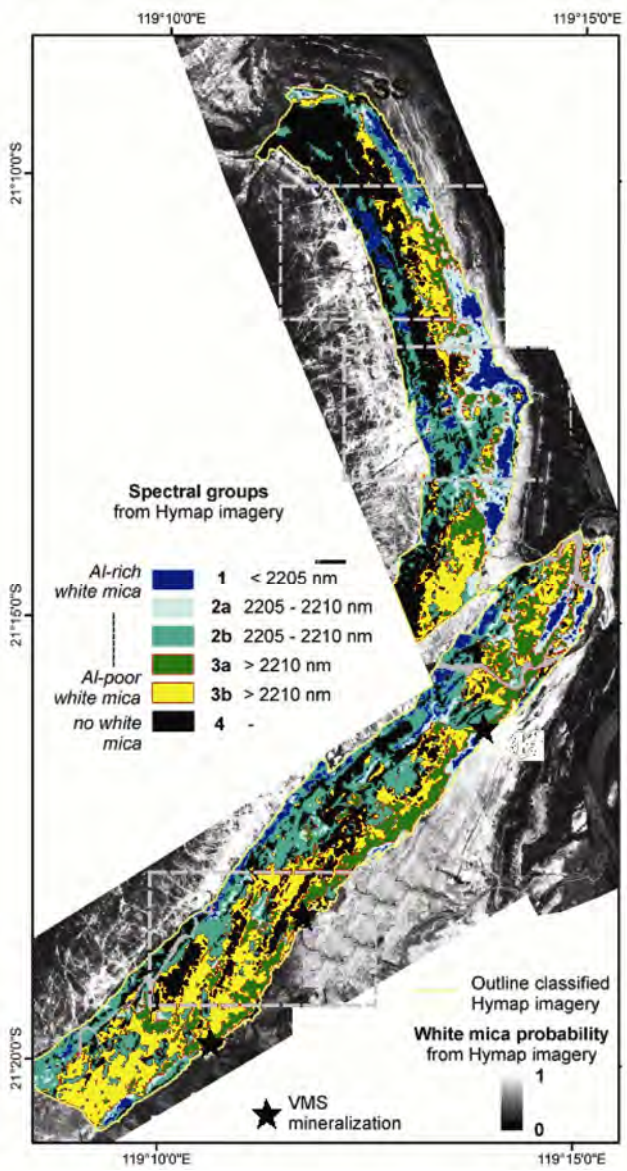

Figure 5. Mapping of white mica minerals using HyMap, Pilbara craton, Australia (after Van Ruitenbeek *et al.*[95]).

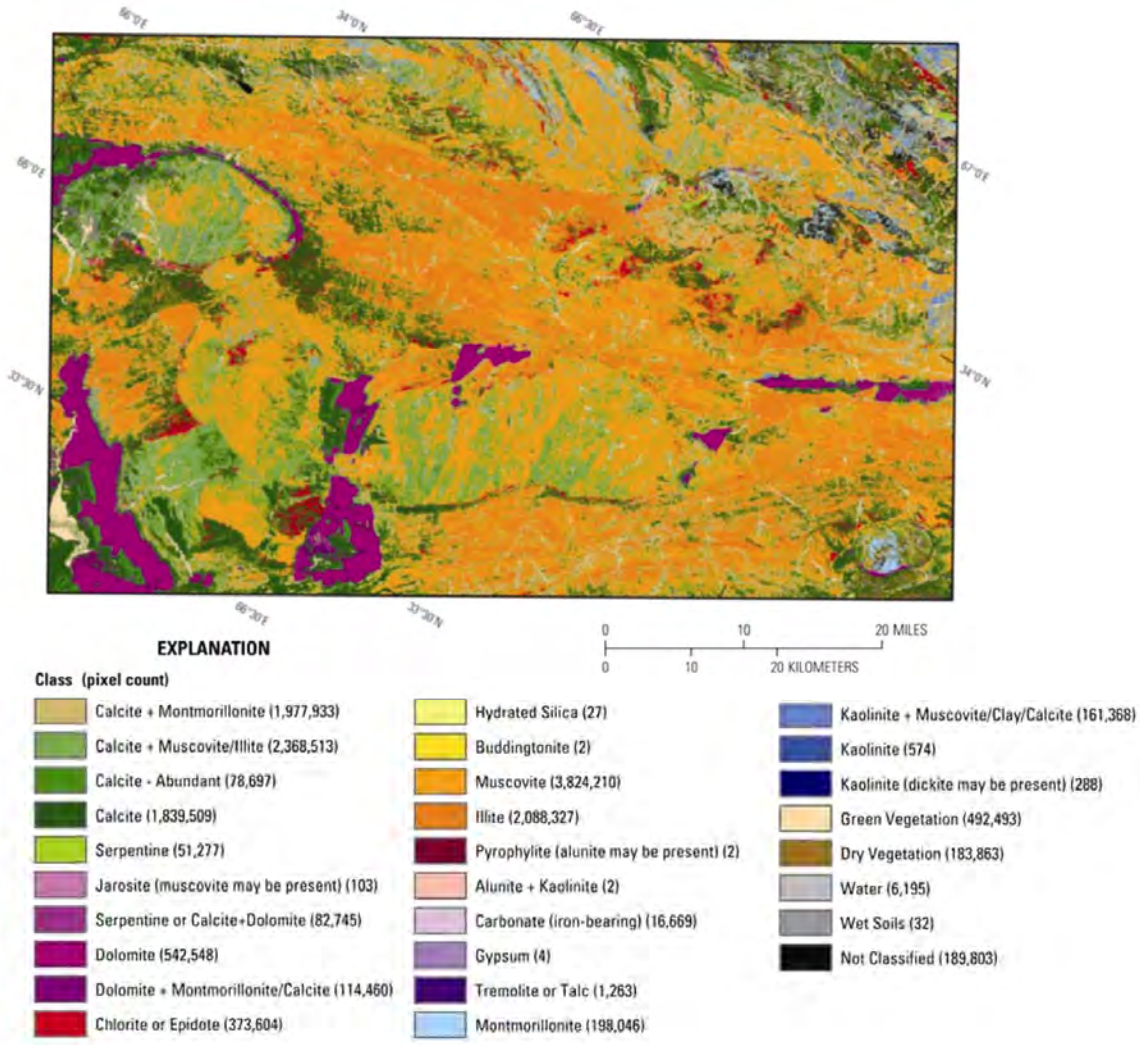

Figure 6. Map of carbonates, phyllosilicates, sulphates, altered minerals, and ore materials derived from HyMap data in Daykundi area, Afghanistan (after Hoefen *et al.*[96]).

Afghanistan (Figure 6) to explore huge Sn–W mineralization and associated alteration zones. Predominant alteration zones that could be mapped using HyMap and field spectroscopy include albitization, silicification, limonitization, bleaching and dickitization. Alteration minerals closely associated with mineralization are chlorite, epidote, kaolin and iron-bearing carbonates. Dominant ore minerals include scheelite, wolframite, pyrite, chalcopyrite, bornite and cassiterite.

Application of HRS on exploration of porphyry-type deposits in various geological settings is well established[77,80,97]. Ever since the first flight of 64-channel airborne spectral profiler over Porphyry Copper Deposit (PCD) of Grapevine Mountains (NGM), Nevada, utility of HRS on exploration of porphyry copper is well known[42]. PCDs are typically characterized by hydrothermal alteration zones with a core of potassic–biotitic, surrounded by phyllic, argillic and propylitic zones. Differentiation among these zones, particularly phyllic and potassic is an important criterion for targeting high economic deposits. These minerals are active in the SWIR region and can be easily deciphered. Central Iranian Volcano-Sedimentary Complex is one of the best sites for understanding PCD-related alteration. Characteristic alteration minerals identified using Hyperion data[77] include biotite, muscovite, illite, kaolinite, goethite, hematite, jarosite, pyrophyllite and chlorite. Besides conventional alteration minerals (kaolinite, dickite, illite, sericite, chlorite and epidote) mapping ammonium–illite has been observed as an excellent tool for orogenic gold deposits[98]. Recent works have shown a relationship between gold mineralization at depth, hydrothermal fluid conduits and ammonium illite on the surface, thus stressing the importance of ammonium illite as a vital tool for different types of epigenetic gold[99].

Among minerals of epigenetic origin, exploring unconformity-related uranium is important due to increasing demand for energy. Diagnosable spectral absorption

features of uranium minerals are confined to 0.40–0.54 μm, 2.1–2.5 μm and 9–14 μm. Typical hydrothermal alterations associated with this mineralization include alkali metasomatism, hematitization, chloritization, silication and fluoritization, and most of the minerals associated with these alteration zones are active in the VNIR–SWIR regions. Studies relating to application of hyperspectral technique on exploration of these deposits include Gardner Range area, Australia[100].

Residual and secondary enrichment deposits: Deposits such as bauxite; lateritic–nickel–cobalt; supergene gold, copper and calcrete-hosted uranium fall under this category. HRS has been used effectively to identify secondary mineral components constituting regolith[1,101,102]. Kusuma *et al.*[1] used field spectroscopic, geochemical, and Hyperion data to precisely map high aluminous bauxites in Konkan region of India. Spectral absorption depths and linear unmixing techniques were used to map different grades of bauxite. Minerals of gossans or iron hats (goethite, hematite, limonite, kaolinite and alunite) and associated supergene enrichment zones (argillic/phosphate/sulphate) are active in the VNIR and SWIR regions and can be mapped using HRS technique[2,98]. Palaeochannels/playas containing groundwater-type calcretes are found to be one of the potential hosts for economic carnotite mineralization[75,103,104].

Hydrocarbon exploration

Though present-generation hydrocarbon reservoirs are deep-seated, adequate fingerprints of their existence in depth can be inferred from manifestation such as seepages and micro-seepages[105]. In recent times, studying surface symptoms of microseepages is gaining importance as a prospective tool for oil and gas exploration. Such exploration adopts direct- and indirect-evidence detection. Direct detection involves mapping/identification of oil pools and alteration of minerals in soils and rocks due to seepages. Indirect detection aims at recognition of secondary effects of volatile hydrocarbons on plants/crops. In both cases, hyperspectral data collected from field/air/space can be of vital importance.

Some of the most promising spectral features and causative molecules include (a) 1.39–1.41 μm due to O–H overtone and C–H combinations; (b) 1.72–1.73 μm absorptions due to combination of CH_3 and CH_2 stretching, (c) CH_2 vibration overtone at 1.75–1.76 μm, (d) combinations of CH_3 asymmetric and symmetric axial deformations and CH_2 symmetric deformation at 2.31 μm and (e) 2.35 μm, absorption due to combination of CH_3 symmetric axial deformation and CH_3 symmetric angular deformation[106]. Petrovic *et al.*[107] presented an exhaustive account of hydrocarbon microseepage-related alteration in soil mineralogy of Lisbon valley, Utah, USA. Reduction of hematite to pyrite and advanced alteration of feldspar, higher concentration of Mo and bleaching of ferruginous sandstone are typical causes of hydrocarbon microseepages. Overall decrease of sulphate and increase of carbonate contents can also be attributed to hydrocarbon[108].

Similar to volatile hydrocarbons seeping from subsurface oil/gas reservoirs, coal-bearing areas also have their own spectral imprints (Figure 7). In the 0.3–2.6 μm region, distinct absorption at 1.4, 1.9 and 2.1–2.6 μm regions appears in low grade coals. Cloutis[109] used reflectance spectra of different types of coal in the 1.8–4 μm region for retrieving both organic and inorganic components. From this work, it is evident (Table 2, Figure 8) that quantitative spectral–compositional relationships are possible, based on which coal properties such as aromaticity, total aliphatic, aromatic content, moisture content, volatile content, fixed carbon abundance, fuel ratio, carbon content, nitrogen abundance, H/C ratio and vitrinite reflectance can be identified.

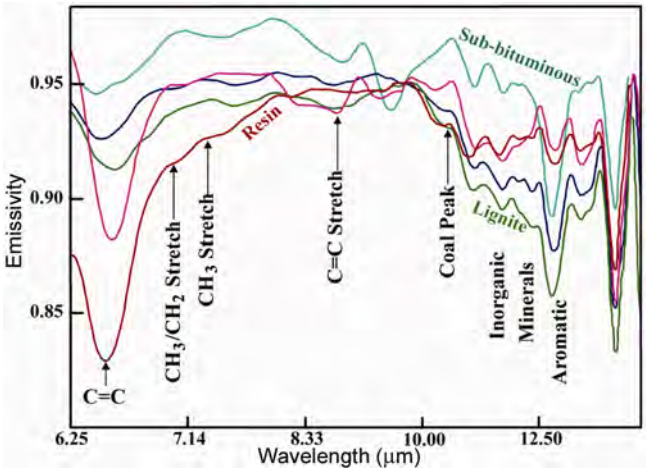

Figure 7. Spectral absorption features due to different organic compounds in different grades of coal.

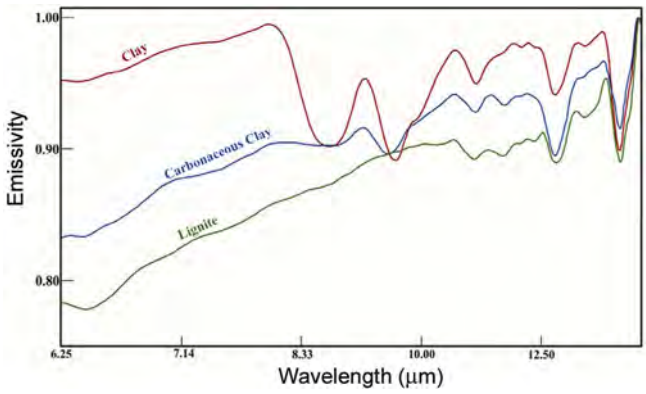

Figure 8. Changes in spectral pattern of coal with progressive increase in inorganic content.

Table 2. Spectral absorption positions and physico-chemical properties of coals

Coal property	Spectral correlation*
Aromaticity factor	3.41 μm-ABD 3.41/3.28 μm-ABDR
Aliphatic (CH + CH_2 + CH_3) content	3.41 μm-ABD
Aromatic C content	3.41/3.28 μm-ABDR 3.28 μm-ABD : ARR
Moisture content	1.9 μm-ABD 2.9 μm-ABD
Volatile content	2.31 μm-ABD 3.41 μm-ABD 3.41/3.28 μm-ABDR
Fixed carbon content	3.41 μm-ABD 3.41/3.28 μm-ABDR 3.28 μm-ABD : ARR
Fuel ratio	3.41/3.28 μm-ABDR 2.31/3.28 μm-ABDR
Carbon content	3.28 μm-ABD : ARR 3.41/3.28 μm-ABDR
Hydrogen content	3.41 μm-ABD : ARR 2.9 + 3.41 μm-ABD
Nitrogen content	7.26 μm-ABD
Oxygen content	1.9 μm-ABD 2.9 μm-ABD
H/C ratio	3.41 μm-ABD 3.41/3.28 μm-ABDR
Vitrinite mean reflectance	3.41 μm-ABD 3.41/3.28 μm-ABDR
Calorific value	3.28 μm-ABD : ARR
Petrofactor	1.6 μm-ARR 3.41/3.28 μm-ABDR

*ABD, Absorption band depth; ABDR, absorption bands depth ratio; ARR, absolute reflectance ratio.

Recent developments and future directions

It is evident from the foregoing sections that hyperspectral imaging has evolved significantly over the last four decades and is being used extensively for mineral targeting/exploration. Advancements in sensor, platform and computing technologies during the last couple of years enabled transformation of HRS to Ultra Spectral Remote Sensing (USRS). Considering the success of Hyperion, seven spaceborne hyperspectral missions (EnMAP, HISUI, HyspIRI, PRISMA, HYPXIM, MSMI and HERO) are planned during 2015–2018. Recent progress in electronics has resulted in the development of micro-, and nano-hyperspectral imagers for small, hand-launched unmanned aerial vehicles. These systems facilitate data acquisition with spectral resolution ranging from 2 to 9 nm and spatial resolution of the order of a few centimetres. Such fine-resolution data alone can resolve spectral features of closely resembling minerals (e.g. ammonium illite and illite), which are otherwise difficult to discern with conventional hyperspectral imagers. These sensors can also play a pivotal role in upscaling spectral details from ground to satellite scales.

The above developments in achieving fine spatio-spectral data would obviously add to data size and dimensionality. This in turn will affect computational efficiency and it is necessary to develop novel image-processing techniques. To address these constraints, it is necessary to design parallel and distributed systems for hyperspectral image analysis. Object-oriented spectral processing and target detection algorithms may be necessary to process ultra-spectral data for real-time compositional mapping/ore grade discrimination. Advancements in sensor and computational techniques are expected to drive all components of HRS from calibration to mapping through steps in between. In brief, HRS will lead to USRS which will revolutionize geological exploration for several decades to come.

1. Kusuma, K. N., Ramakrishnan, D. and Pandalai, H. S., Spectral pathways for effective delineation of high-grade bauxites: a case study from the Savitri River Basin, Maharashtra, India, using EO-1 Hyperion data. *Int. J. Remote Sensing*, 2012, **33**(22), 7273–7290.
2. Ramakrishnan, D., Nithya, M., Singh, K. D. and Bharti, R., A field technique for rapid lithological discrimination and ore mineral identification: results from Mamandur polymetal deposit, India. *J. Earth Syst. Sci.*, 2013, **122**(1), 1–14.
3. Coll, C., Caselles, V., Valor, E., Niclos, R., Sanchez, J. M., Galve, J. M. and Mira, M., Temperature and emissivity separation from ASTER data for low spectral contrast surfaces. *Remote Sensing Environ.*, 2007, **110**, 162–175.
4. Hewson, R. D., Cudahy, T. J., Mizuhiko, S., Ueda, K. and Mauger, A. J., Seamless geological map generation using ASTER in the Broken Hill-Curnamona province of Australia. *Remote Sensing Environ.*, 2005, **99**, 159–172.
5. Tommaso, I. D. and Rubinstein, N., Hydrothermal alteration mapping using ASTER data in the Infiernillo porphyry deposit, Argentina. *Ore Geol. Rev.*, 2007, **32**, 275–290.
6. Goetz, A. F. H., Vane, G., Solomon, J. E. and Rock, B. N., Imaging spectrometry for Earth remote sensing. *Science*, 1985, **228**, 1147–1153.
7. Kruse, F. A., Boardman, J. W. and Huntington, J. F., Comparison of airborne hyperspectral data and EO-1 Hyperion for mineral mapping. *IEEE Trans. Geosci. Remote Sensing*, 2003, **41**(6), 1388–1400.
8. Zhang, X. and Pazner, M., Comparison of lithologic mapping with ASTER, Hyperion, and ETM data in the Southeastern Chocolate Mountains, USA. *Photogramm. Eng. Remote Sensing*, 2007, **73**(5), 555–561.
9. Sturm, B., Atmospheric and radiometric corrections for imaging spectroscopy. In *Imaging Spectroscopy: Fundamentals and Prospective Applications*, Kluwer, The Netherlands, 1992, pp. 47–60.
10. Burns, R., *Mineralogical Applications of Crystal Field Theory*, Cambridge University Press, Cambridge, 1970, p. 551.
11. Hunt, G. R. and Salisbury, J. W., Visible and near infrared spectra of minerals and rocks: I. Silicate minerals. *Mod. Geol.*, 1970, **1**, 283–300.
12. Adams, J. B., Interpretation of visible and near infrared diffuse reflectance spectra of pyroxenes and other rock forming minerals.

In *Infrared and Raman Spectroscopy of Lunar and Terrestrial Minerals* (ed. Karr, C.), Academic Press, California, 1975, pp. 94–116.
13. Burns, R., *Mineralogical Applications of Crystal Filed Theory*, Cambridge University Press, Cambridge, 1993, 2nd edn, p. 551.
14. Clark, R. N., Spectroscopy of rocks and minerals, and principles of spectroscopy. In *Remote Sensing for the Earth Sciences* (ed. Renez, A. N.), John Wiley, New York, 1999, vol. 3, pp. 3–58.
15. Clark, R. N., Swayze, G. A. and Gallagher, A., Mapping the mineralogy and lithology of Canyonlands, Utah with imaging spectrometer data and the multiple spectral feature mapping algorithm. In Summaries of the Third Annual JPL Airborne Earth Science Workshop, Jet Propulsion Laboratory, USA, 1992.
16. Gaffey, S. J., McFadden, L. A., Nash, D. and Pieters, C. M., Ultraviolet, visible and near infrared reflectance spectroscopy: laboratory spectra of geologic materials. In *Remote Chemical Analysis: Elemental and Mineralogical Composition* (eds Pieters, C. M. and Englert, P. A. J.), Cambridge University Press, Cambridge, 1993, pp. 43–78.
17. Hunt, G. R., Spectral signatures of particulate minerals, in the visible and near-infrared. *Geophysics*, 1977, **42**, 501–513.
18. Hunt, G. R., Spectroscopic properties of rocks and minerals. In *Handbook of Physical Properties of Rocks* (ed. Carmichael, R. S.), CRC Press, 1982, pp. 295–385.
19. Hunt, G. R. and Salisbury, J. W., Visible and near infrared spectra of minerals and rocks. II. Carbonates. *Mod. Geol.*, 1971, **2**, 23–30.
20. Salisbury, J. W., Walter, L. S., Vergo, N. and D'Aria, D. M., *Infrared (2.1–2.5 μm) Spectra of Minerals*, Johns Hopkins University Press, Baltimore, 1991, pp. 1–267.
21. Goetz, A. F. H., Curtiss, B. and Shiley, D. A., Rapid gangue mineral concentration measurement over conveyors by NIR reflectance spectroscopy. *Miner. Eng.*, 2009, **22**, 490–499.
22. Kruse, F. A., Identification and mapping of minerals in drill core using hyperspectral image analysis of infrared reflectance spectra. *Int. J. Remote Sensing*, 1996, **17**(9), 1623–1632.
23. Herrmann, W., Blake, M., Doyle, M., Huston, D., Kamprad, J., Merry, N. and Pontual, S., Short wavelength infrared (SWIR) spectral analysis of hydrothermal alteration zones associated with base metal sulphide deposits at Rosebery and Western Tharsis, Tasmania, and Highway-Reward, Queensland. *Econ. Geol.*, 2001, **96**, 939–955.
24. Hook, S. J. and Kahle, A. B., The micro Fourier Transform Interferometer (μFTIR) – a new field spectrometer for acquisition of infrared data of natural surfaces. *Remote Sensing Environ.*, 1996, **56**, 172–181.
25. Wadsworth, W. and Dybwad, J. P., Rugged high-speed rotary imaging Fourier transform spectrometer for industrial use. In Proceedings of SPIE 4577, Vibrational Spectroscopy-based Sensor Systems, 2002, p. 83.
26. Thompson, A. J. B. and Thompson, J. F. H., Atlas of alteration: a field and petrographic guide to hydrothermal alteration minerals. Geological Association of Canada, Mineral Deposits Division, 1996, p. 119.
27. Slater, P. N., Radiometric considerations in remote sensing. *Proc. IEEE*, 1985, **73**, 997–1011.
28. Milton, E. J., Principles of field spectroscopy. *Int. J. Remote Sensing*, 1987, **8**, 1807–1827.
29. Milton, E. J., Rollin, E. M. and Emery, D. R., Advances in field spectroscopy. In *Advances in Environmental Remote Sensing* (eds Danson, F. M. and Plummer, S. E.), John Wiley, Chichester, 1995, pp. 9–32.
30. Kurz, T. H., Integration of ground-based hyperspectral and lidar scanning in virtual outcrop geology. Dissertation, Philosophiae doctor (Ph D), University of Bergen, 2011.
31. Kruse, F. A., Mapping surface mineralogy using imaging spectrometry. *Geomorphology*, 2012, **137**(1), 41–56.
32. Murphy, R. J. and Monteiro, S. T., Mapping the distribution of ferric iron minerals on a vertical mine face using derivative analysis of hyperspectral imagery (430–970 nm). *ISPRS J. Photogramm. Remote Sensing*, 2013, **75**, 29–39.
33. Clark, R. N. *et al.*, Surface reflectance calibration of terrestrial imaging spectroscopy data: a tutorial using AVIRIS. In Proceedings of the 10th Airborne Earth Science Workshop, JPL Publ., 02-1, Pasadana, CA, 2002.
34. Moran, M. S., Jackson, R. D., Slater, P. N. and Teillet, P. M., Evaluation of simplified procedures for retrieval of land surface reflectance factors from satellite sensor output. *Remote Sensing Environ.*, 1992, **41**, 169–184.
35. Milton, E. J., Schaepman, M. E., Anderson, K., Kneubühler, M. and Fox, N., Progress in field spectroscopy. *Remote Sensing Environ.*, 2009, **113**, S92–S109.
36. Van Der Meer, F. D. *et al.*, Multi- and hyperspectral geologic remote sensing: a review. *Int. J. Appl. Earth Obs. Geoinf.*, 2012, **14**(1), 112–128.
37. Bharti, R., Ramakrishnan, D., Singh, K. D. and Nithya, M., Relevance of mineral texture on bidirectional reflectance and emission spectroscopy: implications for geological remote sensing. IEEE International Geoscience and Remote Sensing Symposium (IGARSS), 2012, pp. 3046–3049.
38. Clark, R. N., Swayze, G. A., Wise, R., Livo, K. E., Hoefen, T. M., Kokaly, R. F. and Sutley, S. J., USGS Digital Spectral Library splib05a. US Geological Survey, Open File Report 03-395, 2003.
39. Christensen, P. R. *et al.*, A thermal emission spectral library of rock-forming minerals. *J. Geophys. Res. (Planets) E4*, 2000, **105**, 9735–9739.
40. Ramakrishnan, D., Radhika, N., Singh, K. D. and Bharti, R., A fast procedure for field and satellite spectral deconvolution and its ramification in automated detection of materials. In Proceedings of GeoSummit, Sathyabhama University, Chennai, 27–29 July 2011.
41. Roberts, D. A., Yamaguchi, Y. and Lyon, R., Comparison of various techniques for calibration of AIS data. In Proceedings of the 2nd Airborne Imaging Spectrometer Data Analysis Workshop (eds Vane, G. and Goetz, A. F. H.), JPL Publ., Pasadena, CA, 1986, vol. 86(35), pp. 21−30.
42. Kruse, F. A., Use of airborne imaging spectrometer data to map minerals associated with hydrothermally altered rocks in the northern Grapevine Mountains, Nevada and California. *Remote Sensing Environ.*, 1988, **24**(1), 31–51.
43. Conel, J. E., Green, R. O., Vane, G., Bruegge, C. J. and Alley, R. E., AIS-2 radiometry and a comparison of methods for the recovery of ground reflectance. In Proceedings of the 3rd Airborne Imaging Spectrometer Data Analysis Workshop (ed. Vane, G.), JPL, Publ., Pasadena, CA, 1987, **87**(30), 18–47.
44. Gao, B. C., Montes, M. J., Davis, C. O. and Goetz, A. F. H., Atmospheric correction algorithms for hyperspectral remote sensing data of land and ocean. *Remote Sensing Environ.*, 2009, **113**, S17–S24.
45. Gao, B. C., Heidebrecht, K. B. and Goetz, A. F. H., Derivation of scaled surface reflectances from AVIRIS data. *Remote Sensing Environ.*, 1993, **44**, 165–178.
46. Qu, Z., Kindel, B. C. and Goetz, A. F. H., The high accuracy atmospheric correction for hyperspectral data (HATCH) model. *IEEE Trans. Geosci. Remote Sensing*, 2003, **41**, 1223–1231.
47. Kruse, F. A., Comparison of ATREM, ACORN, and FLAASH atmospheric corrections using low-altitude AVIRIS data of Boulder, CO. In Summaries of 13th JPL Airborne Geoscience Workshop, Jet Propulsion Lab, Pasadena, CA, 2004.
48. Adler-Golden, S. M. *et al.*, Atmospheric correction for shortwave spectral imagery based on MODTRAN4. *Proc. SPIE*, 1999, **3753**, 61–69.
49. Staenz, K., Szeredi, T. and Schwarz, J., ISDAS – a system for processing/analyzing hyperspectral data; technical note. *Can. J. Remote Sensing*, 1998, **24**, 99–113.

50. Richter, R. and Schlaepfer, D., Geo-atmospheric processing of airborne imaging spectrometry data. Part 2: Atmospheric/ topographic correction. *Int. J. Remote Sensing*, 2002, **23**(13), 2631–2649.
51. Green, A. A., Berman, M., Switzer, P. and Craig, M. D., A transformation for ordering multispectral data in terms of image quality with implications for noise removal. *IEEE Trans. Geosci. Remote Sensing*, 1988, **26**, 65–74.
52. Chiang, S. S., Chang, C. I. and Ginsberg, I. W., Unsupervised hyperspectral image analysis using independent component analysis. In Proceedings of the IEEE: Geoscience and Remote Sensing Symposium, 2000, pp. 3136–3138.
53. Tu, T. M., Chen, C. H. and Chang, C. I., A posteriori least squares orthogonal subspace projection approach to desired signature extraction and detection. *IEEE Trans. Geosci. Remote Sensing*, 1997, **35**, 127–139.
54. Ifarraguerri, A. and Chang, C. I., Multispectral and hyperspectral image analysis with convex cones. *IEEE Trans. Geosci. Remote Sensing*, 1999, **73**(2), 756–770.
55. Keshava, N. and Mustard, J. F., Spectral unmixing. *IEEE Signal Process. Mag.*, 2002, **19**, 44–57.
56. Nascimento, J. M. P. and Bioucas-Dias, J. M., Does independent component analysis play a role in unmixing hyperspectral data? *IEEE Trans. Geosci. Remote Sensing*, 2005, **43**(1), 175–187.
57. Boardman, J. W., Automating spectral unmixing of AVIRIS data using convex geometry concepts. In Summaries of the 4th Annual JPL Air-borne Geoscience Workshop, JPL, Pasadena, CA, 1993, pp. 11–14.
58. Boardman, J. W., Kruse, F. A. and Green, R. O., Mapping target signatures via partial unmixing of AVIRIS data. In Summaries, Fifth JPL Airborne Earth Science Workshop, 1995, pp. 23–26.
59. Plaza, A., Martinez, P., Perez, R. and Plazas, J., Spatial/spectral endmember extraction by multidimensional morphological operators. *IEEE Trans. Geosci. Remote Sensing*, 2002, **40**(9), 2025–2041.
60. Craig, M. D., Minimum-volume transforms for remotely sensed data. *IEEE Trans. Geosci. Remote Sensing*, 1994, **32**(3), 542–552.
61. Hamilton, V. E. and Christensen, P. R., Determination of Martian meteorite lithologies and mineralogies using vibrational spectroscopy. *J. Geophys. Res.*, 1997, **102**, 25593–25603.
62. Hamilton, V. E. and Christensen, P. R., Determining the modal mineralogy of mafic and ultramafic igneous rocks using thermal emission spectroscopy. *J. Geophys. Res.*, 2000, **105**, 9717–9733.
63. Ramsey, M. S. and Christensen, P. R., Mineral abundance determination: quantitative deconvolution of thermal emission spectra. *J. Geophys. Res.*, 1998, **103**, 577–596.
64. Hapke, B. and Wells, E., Bidirectional reflectance spectroscopy: 2. Experiments and observation. *J. Geophys.*, 1981, **86**, 3055–3060.
65. Hapke, B., Bidirectional reflectance spectroscopy: 5. The coherent backscatter opposition effect and anisotropic scattering. *Icarus*, 2002, **157**, 523–534.
66. Hapke, B., Bidirectional reflectance spectroscopy: 3. Correction for macroscopic roughness. *Icarus*, 1984, **59**(1), 41–59.
67. Shepard, M. K. and Campbell, B. A., Shadows on a planetary surface and implications for photometric roughness. *Icarus*, 1998, **134**, 279–291.
68. Cord, A. M., Pinet, P. C., Daydou, Y. and Chevrel, S. D., Planetary regolith surface analogs: optimized determination of Hapke parameters using multi-angular spectro-imaging laboratory data. *Icarus*, 2003, **165**, 414–427.
69. Hapke, B., Nelson, R. and Smythe, W., The opposition effect of the moon: coherent backscatter and shadow hiding. *Icarus*, 1998, **133**, 89–97.
70. Hapke, B., Bidirectional reflectance spectroscopy: 4. The extinction coefficient and the opposition effect. *Icarus*, 1986, **67**, 264–280.
71. Henyey, L. G. and Greenstein J. L., Diffuse radiation in the galaxy. *Astrophys. J.*, 1941, **93**, 70–83.
72. Jacquemoud, S., Baret, F. and Hanocq, J. F., Modeling spectral and bidirectional soil reflectance. *Remote Sensing Environ.*, 1992, **41**, 123–132.
73. Bedini, E., Van der Meer, F. and Van Ruitenbeek, F., Use of HyMap imaging spectrometer data to map mineralogy in the Rodalquilar caldera, southeast Spain. *Int. J. Remote Sensing*, 2009, **30**, 327–348.
74. Mulder, V. L., de Bruina, S., Weyermannb, J., Kokalyc, R. F. and Schaepmana, M. E., Characterizing regional soil mineral composition using spectroscopy and geostatistics. *Remote Sensing Environ.*, 2013, **139**, 415–429.
75. Bharti, R. and Ramakrishnan, D., Uraniferous calcrete mapping using hyperspectral remote sensing. IEEE International Geoscience and Remote Sensing Symposium, 2014, pp. 2902–2905.
76. Kruse, F. A. and Boardman, J. W., Characterization and mapping of kimberlites and related diatremes using hyperspectral remote sensing. *IEEE Trans. Geosci. Remote Sensing*, 2000, **3**, 299–304.
77. Bishop, C. A., Liu, J. G. and Mason, P. J., Hyperspectral remote sensing for mineral exploration in Pulang, Yunnan Province China. *Int. J. Remote Sensing*, 2011, **32**(9), 2409–2426.
78. Kodikara, G. R. L., Woldai, T., van Ruitenbeek, F. J. A., Kuria, Z., van der Meer, F. A., Shepherd, K. D. and van Hummel, G. J., Hyperspectral remote sensing of evaporate minerals and associated sediments in Lake Magadi area, Kenya. *Int. J. Appl. Earth Obs. Geoinf.*, 2012, **14**(1), 22–32.
79. Kusuma, K. N., Ramakrishnan, D., Pandalai, H. S. and Kailash, G., Noise reduction in field spectroradiometer data – the 'noise–signal index threshold' and its significance in hyperspectral image classification: a case study of laterite, lateritic–bauxite and bauxite mapping. *Geocarto Int.*, 2010, **25**(7), 569–580.
80. Zadeh, M. H., Tangestani, M. H., Roldan, F. V. and Yusta, I., Sub-pixel mineral mapping of a porphyry copper belt using EO-1 Hyperion data. *Adv. Space Res.*, 2014, **53**(3), 440–451.
81. Tan, K., Wan, Y., Sun, S., Kuang, J. and Chen, X., Application research on coal prospecting with remote sensing. *Proc. Earth Planet. Sci.*, 2011, **3**, 103–112.
82. Harris, J., Rogge, D., Hitchcock, R., Ijewliw, O. and Wright, D., Mapping lithology in Canada's Arctic: application of hyperspectral data using the minimum noise fraction transformation and matched filtering. *Can. J. Earth Sci.*, 2005, **42**, 2173–2193.
83. Rivard, B., Zhang, J., Feng, J. and Sanchez-Azofeifa, G. A., Remote predictive lithologic mapping in the Abitibi Greenstone Belt, Canada, using airborne hyperspectral imagery. *Can. J. Remote Sensing*, 2009, **35**, S95–S105.
84. Roy, R. *et al.*, Geological mapping strategy using visible near-infrared–shortwave infrared hyperspectral remote sensing: application to the Oman ophiolite (Sumail massif). *Geochem. Geophys. Geosyst.*, 2009, **10**(2), 1–23.
85. Launeau, P., Girardeau, J., Sotin, C. and Tubia, J. M., Comparison between field measurements and airborne visible and infrared mapping spectrometry (AVIRIS and HyMap) of the Ronda peridotite massif (south-west Spain). *Int. J. Remote Sensing*, 2004, **25**(14), 2773–2792.
86. Keeling, J. L., Mauger, A. J. and Raven, M. D., Airborne hyperspectral survey and kimberlite detection in the Terowie district, South Australia. In *Regolith* (ed. Roach, I. C.), CRC LEME, 2004, pp. 166–170.
87. Gupta, R. P., *Remote Sensing Geology*, Springer-Verlag, Berlin, 2003, 2nd edn, pp. 1–656.
88. Salisbury, J. W. and Daria, D. M., Emissivity of terrestrial materials in the 3–5 μm atmospheric window. *Remote Sensing Environ.*, 1994, **47**, 345–361.
89. Merucci, L., Bogliolo, M. P., Buongiorno, M. F., Teggi, S. and Nazionale, I., Spectral emissivity and temperature maps of the

Solfatara crater from DAIS hyperspectral images. *Ann. Geophys.*, 2006, **49**(1), 235–244.
90. Vaughan, R. G., Calvin, W. M. and Taranik, J. V., SEBASS hyperspectral thermal infrared data: surface emissivity measurement and mineral mapping. *Remote Sensing Environ.*, 2003, **85**(1), 48–63.
91. Kurz, T. H., Dewit, J., Buckley, S. J., Thurmond, J. B., Hunt, D. W. and Swennen, R., Hyperspectral image analysis of different carbonate lithologies (limestone, karst and hydrothermal dolomites): the Pozalagua Quarry case study (Cantabria, North-west Spain). *Sedimentology*, 2012, **59**, 623–645.
92. Aubrey, A. *et al.*, Sulfate minerals and organic compounds on Mars. *Geology*, 2006, **34**, 357–360.
93. Langevin, Y., Poulet, F., Bibring, J. P. and Gondet, B., Sulfates in the North Polar region of Mars detected by OMEGA/Mars Express. *Science*, 2005, **307**, 1584–1586.
94. Drieberg, S., The magmatic–hydrothermal architecture of the Archean Volcanic Massive Sulfide (VMS) system at Panorama, Pilbara, Eastern Australia. Ph D, University of Western Australia, 2003.
95. Van Ruitenbeek, F. J. A., Cudahy, T. J., Van der Meer, F. D. and Hale, M., Characterization of the hydrothermal systems associated with Archean VMS-mineralization at Panorama, Western Australia, using hyperspectral, geochemical and geothermometric data. *Ore Geol. Rev.*, 2012, **45**, 33–46.
96. Hoefen, T. M., Knepper Jr, D. H. and Giles, S. A., Analysis of imaging spectrometer data for the Daykundi area of interest. In *Summaries of Important Areas for Mineral Investment and Production Opportunities of Nonfuel Minerals in Afghanistan* (eds Peters, S. G. *et al.*), US Geological Survey, Reston, Virginia, 2011, pp. 314–339.
97. Kruse, F. A., Kierein-Young, K. S. and Boardman, J. W., Mineral mapping at Cuprite, Nevada with a 63-channel imaging spectrometer. *Photogramm. Eng. Remote Sensing*, 1990, **56**(1), 83–92.
98. Bierwirth, P., Huston, D. and Blewett, R., Hyperspectral mapping of mineral assemblages associated with gold mineralization in the Central Pilbara, Western Australia. *Econ. Geol.*, 2002, **97**, 819–826.
99. Mateer, M., Ammonium Illite at the Jerritt Canyon District and Gold strike Property, Nevada: its spatial distribution and significance in the exploration of Carlin-type deposits. Unpublished thesis dissertation. University of Wyoming, 2010.
100. McKay, A. and Miezitis, Y., Australia's uranium resources, geology and development of deposits. AGSO–Geoscience Australia Mineral Report, 2001, vol. 1, pp. 1–200.
101. Papp, E. and Cudahy, T., Hyperspectral remote sensing. In *Geophysical and Remote Sensing Methods for Regolith Exploration* (ed. Papp, E.), Open File Report, 2002, vol. 144, 13–21.
102. Deller, A. M. E., Facies discrimination in laterites using Landsat Thematic Mapper, ASTER and ALI data – examples from Eritrea and Arabia. *Int. J. Remote Sensing*, 2006, **27**, 2389–2409.
103. Bowell, R. J., Booysens, M., Pedley, A., Church, J. and Moran, A., Characterization of carnotite uranium deposit in calcrete channels, Trekkopje, Namibia. In Proceedings of Africa Uncovered: Mineral Resources for the Future. SEG-GSSA 2008 Conference, 2008, pp. 114–121.
104. Ramesh Kumar, K., Misra, A., Pande, D. and Nanda, L. K., Uranium in lake sediments – a report on Didwana Salt Lake, Nagaur District, Rajasthan. *Curr. Sci.*, 2009, **97**(11), 1545–1546.
105. Van der Meer, F. D. *et al.*, An integrated geoscience approach for hyperspectral hydrocarbon microseepage detection. In Proceedings of the 14th International Conference on Applied Geologic Remote Sensing, Environmental Research Institute on Michigan (ERIM), Las Vegas, Nev., USA, 2000, pp. 81–88.
106. Lammoglia, T. and Filho, C. R. S., Spectroscopic characterization of oils yielded from Brazilian offshore basins: potential applications of remote sensing. *Remote Sensing Environ.*, 2011, **115**, 2525–2535.
107. Petrovic, A., Khan, S. D. and Thurmond, A. K., Integrated hyperspectral remote sensing, geochemical and isotopic studies for understanding hydrocarbon-induced rock alterations. *Mar. Petr. Geol.*, 2012, **35**(1), 292–308.
108. Tangestani, M. H. and Validabadi, K., Mineralogy and geochemistry of alteration induced by hydrocarbon seepage in an evaporite formation; a case study from the Zagros Fold Belt, SW Iran. *Appl. Geochem.*, 2014, **41**, 189–195.
109. Cloutis, E. A., Quantitative characterization of coal properties using bidirectional diffuse reflectance spectroscopy. *Fuel*, 2003, **82**(18), 2239–2254.

ACKNOWLEDGEMENTS. We acknowledge all earlier contributions on this subject. Efforts were taken to cite most of relevant works.